PHYSICS OF FLUIDS **26**, 115101 (2014)

A dynamic end cap technique for sound computation using the Ffowcs Williams and Hawkings equations

Zane Nitzkorski and Krishnan Mahesh
Department of Aerospace Engineering and Mechanics, University of Minnesota, Minneapolis, Minnesota 55455, USA

(Received 30 June 2014; accepted 21 October 2014; published online 10 November 2014)

A dynamic end cap methodology is proposed to account for spurious contributions to the far-field sound within the context of the Ffowcs–Williams and Hawkings (FW–H) acoustic analogy. The quadrupole source terms are correlated over multiple planes to obtain a convection velocity which is then used to determine a corrective convective flux at the FW–H porous surface. The proposed approach is first demonstrated for a convecting potential vortex. It is then evaluated by computing the sound emitted by flow over circular cylinders at Reynolds number of 150, 10 000, and 89 000, respectively. The low Re cylinder is used to validate against direct numerical simulation (DNS) and demonstrate insensitivity to end plane location and spacing, the effect of dynamic convection velocity and to compare to commonly used end cap corrections. The Re 100 00 cylinder is used to validate at turbulent Reynolds numbers against other simulations. Finally the Re 89 000 simulations are used to compare to experiment. The proposed approach demonstrates better performance than other commonly used approaches with the added benefit of computational efficiency and the ability to query independent volumes. © *2014 AIP Publishing LLC*. [http://dx.doi.org/10.1063/1.4900876]

I. INTRODUCTION

The generation of noise in most practical applications involving fluid flow is the result of turbulence interacting with a physical body which scatters, reflects, and converts fluid energy into acoustic energy. This mechanism produces many tonal and broadband frequencies that have significant acoustic content which depend on geometry and nature of the flow field. The large difference in the energy and length scales associated with the flow field and the acoustic field make it difficult to directly compute the the far-field sound. An acoustic analogy is a rearrangement of the Navier-Stokes equations into an inhomogeneous wave equation which can be solved with the use of Greens functions to analytically project the solution for the acoustic pressure or density to any point of interest, thus avoiding any dissipation or dispersion errors associated with direct computational methods. Lighthill[1] originally derived the wave equation that serves as the basis for many acoustic analogies and applied it to free shear flows. Curle[2] and then Ffowcs-Williams and Hawkings[3] extended this methodology to include stationary surfaces and moving surfaces, respectively, by incorporating additional forcing terms to the wave equation. The Ffowcs-Williams and Hawkings approach can be applied for non-rigid or porous surfaces in motion that can encapsulate a section of the flow field, thus naturally decoupling the hydrodynamic near field from the acoustic far field. There are many integral approaches, such as Kirchhoff surfaces, that qualify as acoustic analogies as discussed by Lyrintzis,[4] but the FW−H approach is preferable because it is more robust at capturing nonlinear affects with respect to choice of surface location, e.g., Brentner and Farassat.[5]

Acoustic analogies involve a variety of assumptions about acoustic compactness, importance of geometry, and solution domain. The formulaic basis for most FW−H implementations is thoroughly derived by Brentner and Farassat;[6] it involves an arbitrary data surface located at $f = 0$ and is

expressed as

$$\left(\frac{1}{c^2}\frac{\partial^2}{\partial t^2}-\nabla^2\right)p'(x,t)=\frac{\partial}{\partial t}\left\{Q_i n_i \delta(f)\right\}-\frac{\partial}{\partial x_i}\left\{L_{ij}n_j\delta(f)\right\}+\frac{\partial^2}{\partial x_i \partial x_j}\left\{T_{ij}H(f)\right\}, \quad (1)$$

where

$$Q_i=\rho_0 v_i+\rho(u_i-v_i),\ L_{ij}=\rho u_i(u_j-v_j)+P_{ij},\ \text{and}\ T_{ij}=\rho u_i u_j+P_{ij}-c_0^2(\rho-\rho_0). \quad (2)$$

T_{ij} is known as the Lighthill stress tensor. Here, u_n is the local value of the fluid velocity at the surface, v_n is the local velocity of the surface, $P_{ij}=(p-p_0)\delta_{ij}-\tau_{ij}$ is the compressive stress tensor including viscous stresses, and all reference quantities are specified with respect to a quiescent background. Equation (1) is an inhomogeneous wave equation that is solved using an integral representation involving Greens functions. Any mean background flow or motion may also be represented by rearranging these terms depending on the frame of reference as shown by Casalino[7] or Najafi-Yazdi *et al.*[8] An integral solution of this differential equation is used to recover the acoustic pressure, for which Farassat[9] details possible bounds of integration. For example, the three dimensional retarded time formulation utilizes the Greens function

$$G(\mathbf{x},\mathbf{y},t-\tau)=\frac{1}{4\pi|x-y|}\delta\left(t-\tau-\frac{|x-y|}{c_0}\right), \quad (3)$$

where y, τ are the emission or source and x, t are the receiver location and time. Applying Eq. (3) to Eq. (1) and integrating both sides of the wave equation results in

$$p'(x,t)=\frac{\partial^2}{\partial x_i\partial x_j}\int_{V_{ext}}\frac{[T_{ij}]}{4\pi|x-y|}\mathrm{d}^3\mathrm{y}-\frac{\partial}{\partial x_i}\int_S\frac{[\rho u_i(u_n-v_n)+P_{ij}n_j]}{4\pi|x-y|}\mathrm{dS}+\frac{\partial}{\partial t}\int_S\frac{[\rho_0 v_n+\rho(u_n-v_n)]}{4\pi|x-y|}\mathrm{dS}. \quad (4)$$

Here, it has been assumed that the retarded time, $\tau=t-\frac{|x-y|}{c}$, and delta functions enforce that the bracketed terms are evaluated at their retarded source times. Additional simplification can be achieved if a compact source region is assumed as shown by Howe[10] or Goldstein.[11] Compactness yields $|x-y|\approx|x|$ to finally obtain

$$p'(x,t)=\frac{x_i x_j}{4\pi c_0^2|x|^3}\frac{\partial^2}{\partial t^2}\int_{V_{ext}}[T_{ij}]\mathrm{d}^3\mathrm{y}+\frac{x_i}{4\pi c_0|x|^2}\frac{\partial}{\partial t}\int_S[\rho u_i(u_n-v_n)+P_{ij}n_j]\mathrm{dS}+\frac{1}{4\pi|x|}\frac{\partial}{\partial t}\int_S[\rho_0 v_n+\rho(u_n-v_n)]\mathrm{dS}. \quad (5)$$

The three terms have physically relevant meanings if the data surface $f=0$ is aligned with a physical boundary. They are then termed the volume, loading, and displacement thickness or equivalently the quadrupole, dipole, and monopole terms. In the case where there is zero penetration into the body and in a body fixed frame $u_n=v_n=0$, we recover a standard Curle type formulation where only stresses acting on the body as well as turbulent self-interaction in the neighboring region generate recovered noise. It should be noted that shifts in frequency and amplitude due to relative motion or Doppler shift are handle by the introduction of the radiated Mach number, $1-M$, in the denominator of each integrand per polar expansion. This approach is different from the common retarded time implementation of Brentner and Farassat's 1A formulation where the volume term is dropped, the time derivatives are brought into integrals, and the polar expansion results in the dot product with radiation vectors. This paper uses Eq. (5) to implement the FW–H methodology. The assumptions of compactness and the retarded time formulation restrict its validity to low Mach number flows.

A. "END CAP" PROBLEM

The volume term can be computationally expensive to retain, and difficult to compute. A related problem is the choice of Greens' function which dictates propagation exterior to the bounding surface. If the porous surface is near or at the physical surface the Greens' function should account

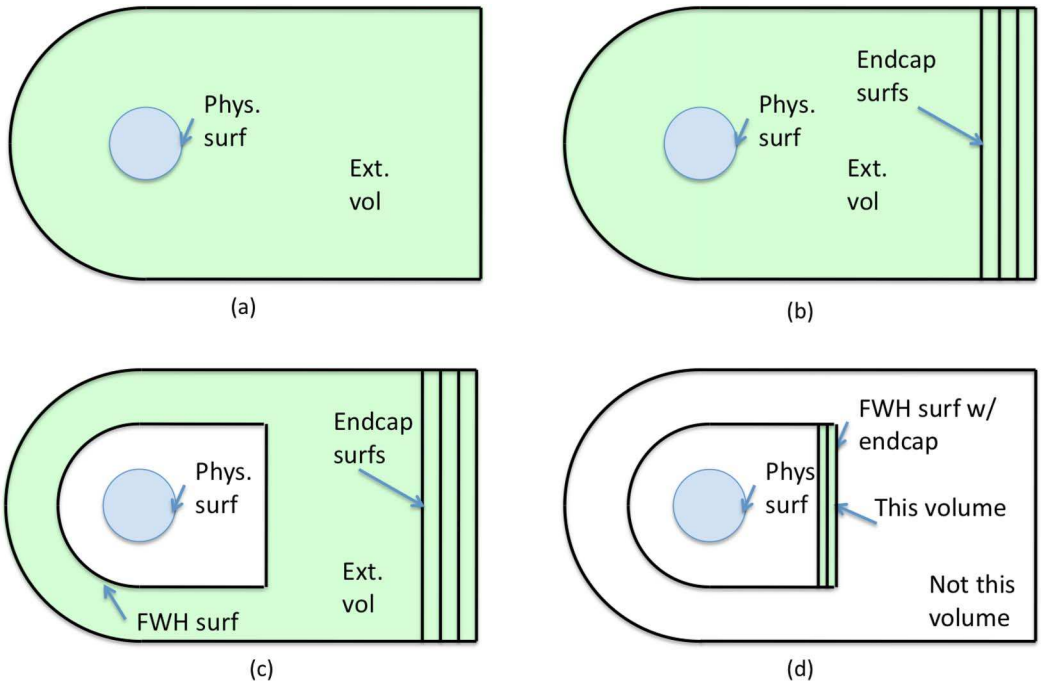

FIG. 1. A schematic emphasizing various decomposition approaches. (a) Computational approach where the surface is the physical surface and the entire computational domain is the exterior volume; undamped fluctuating velocities at an exit of the volume can cause spurious noise. (b) End cap correction concept for exit plane. (c) The porous surface is the data surface and the volume has end cap correction. This is computationally inefficient as volume sources are small and costly to compute. (d) Computational efficiency is gained by effectively neglecting the noise production from volume sources while retaining appropriate closure.

for the geometry; if it is sufficiently far away, a free space Greens function may be assumed but handling volume terms become important. The volume terms pose what is termed as the "end cap" or closure problem. When examining the volume term it is clear that some practical limit to the size of domain must be established, and when an undamped acoustic source exits the zone of integration, there will be a discrete spike in the received noise for no reason other than the finite size of the domain. An example where surface source terms are interrelated and non-unique is given in Ref. 6. Furthermore, Ffowcs Williams[12] clearly detailed how surface and volume terms are interrelated and nonlinearity is expressed depending on the data surface location. The surface terms end up directly relating to the volume terms and vice-versa in that if an uncorrected error occurs in one term it can be rearranged to instead appear in the other. A variety of approaches are used to appropriately close the integration boundary or correct the porous surface terms (Figure 1). The first approach is to ignore the volume term by assuming it to be small and instead only use the physical surfaces where penetrating sound sources do not exist. The next approach is to not enclose the back of domain where the problem is manifest, e.g., wake of bluff body, while including other faces of the porous surface. This approach under predicts the noise in radiation directions that are bounded by the normals of the missing surface. The third approach is phase averaging of the noise contributions over a series of exit plane as suggested by Shur *et al.*[13] The idea is that if there are enough well-spaced planes the error at each station should be phased shifted relative to the others and that by averaging the complex signal, the average should have lower overall error.

In this paper, we develop a methodology for end cap correction that uses corrected volume terms, along with multiple exit planes to dynamically calculate correction parameters. The proposed method allows efficient computation of the volume terms, querying of independent volumes, is insensitive to the location of the end cap planes, and is more accurate than the previously discussed approaches. The proposed approach is based on the concept of multiple exit planes over which the flux of quadrupole terms are subtracted and correlated. The exit flux concept was first suggested by

Wang *et al.*[14] in the context of the volume terms with nonporous body-aligned FW–H surfaces and a fixed empirical velocity at the exit of the computational domain in order to deal with spurious, undamped volume noise. Here, we apply it in the context of the FW–H methodology specifically as a correction for porous surfaces in the near field along with a dynamic approach to compute the convection velocity by correlating the source terms over multiple planes. The paper is organized as follows. Section II describes the proposed dynamic methodology for end cap correction and evaluates its promise by applying it to a two-dimensional vortex advecting across a FW–H porous surface. This is followed by simulations of the flow around circular cylinders, and computation of the emitted far–field noise. A description of the numerical method in Sec. III is followed by results in Sec. IV. Three Reynolds numbers are considered: 150, 10 000, and 89 000. The low Re cylinder flow is used to validate against DNS results of directly computed sound, demonstrate insensitivity of the proposed methodology to end plane location and spacing, demonstrate the importance of dynamically computing the convection velocity, and to compare to commonly used end cap correction approaches. The Re 10 000 cylinder is chosen as a turbulent flow which can be compared against other simulations. Finally, the Re 89 000 simulations are used to compare to experiment. A brief summary in Sec. V concludes the paper.

II. PROPOSED METHODOLOGY FOR END CAP CORRECTION

A. Basic idea

Figure 2 shows a schematic of a FW–H porous surface wrapped around a sound source with end cap planes adjacent to one end of the surface. Consider the two volumes V_0 and $V_0 + \Delta V$ that extend exterior to the porous surface. Assume the existence of a background velocity U_c which convects sources over the two differential volumes. A truncation error, E_{ij}, is generated as the source exits each volume. Assuming the sources are largely unchanged across ΔV implies that the truncation error is also unchanged. This means that the differential distance Δy_1 corresponds to a time difference $\Delta\tau = \frac{\Delta y_1}{U_c}$ for the error to be received at a microphone position from each volume. Expressing this error in the first derivative of the volume terms $\dot{T}_{ij}$ and Taylor series expanding yields

$$\dot{T}_{ij}^{\pm} = \dot{T}_{ij} + E_{ij}[t \mp \Delta/2], \tag{6}$$

$$\ddot{T}_{ij}^{+} \approx \frac{1}{2}\left(\ddot{T}_{ij}^{+} + \ddot{T}_{ij}^{-}\right) + \frac{1}{\Delta\tau}\left(\dot{T}_{ij}^{+} + \dot{T}_{ij}^{-}\right) \tag{7}$$

between the larger (+) volume and the smaller (−) volumes. Expressing this in integral form for the total volume noise

$$\ddot{T}_{ij}(t) = \frac{\partial^2}{\partial t^2}\int_{V_0} T_{ij}(y,\tau)\mathrm{d}y^3 + \frac{\partial}{\partial t}\int_{S_{ext}} U_c T_{ij}(y,\tau)\mathrm{d}y^2. \tag{8}$$

The corrective flux $\frac{\partial}{\partial t}\int_{S_{ext}} U_c T_{ij}(y,\tau)\mathrm{d}y^2$ is applied at the exit surface of the bounding volume in order to approximate the missing sources exterior to the surface of integration.

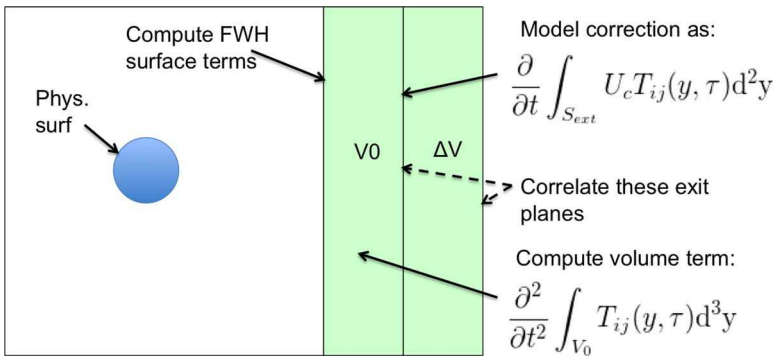

FIG. 2. Schematic representation of the proposed end cap method.

The proposed scheme assumes that the primary cause of the error is due to the convection of a truncation error over a finite domain captured only on the porous FW–H surface. This is eliminated by the inclusion of the volume term which is accurately corrected at its truncation location. This means that the corrected volume term is used as the correction to the finite size FW–H terms. Furthermore, we dynamically calculate the model constant, U_c, by correlating the correction term over subsequent exit planes. The first step is finding a pair of related exit surface elements, indexed as j and k, through a ray tracing routine based on the dot product of the total velocity with the element normal $\hat{n}_k$. The distance between the elements $dx_{j,k}$ establishes a correlation function based on the corrective flux to compute U_c as

$$U_c = \sum_{j=0,k=0}^{N_j,N_k} \frac{dx_{j,k} \cdot \hat{n}_k}{max(\frac{\beta(t)\hat{R}_{xy}(m)}{N})dt}. \tag{9}$$

The multiplying factor $\beta(t)$ is a windowing function in time which ensures only one maximum correlation over any given averaging period. This is then averaged to obtain the average convection velocity between any two surfaces. It is important to note that in the correlation function

$$\hat{R}_{xy}(m) = \begin{cases} \sum_{n=0}^{N-m-1} \alpha x_{n+m}\, y_n^* & m \geq 0 \\ \\ \hat{R}_{xy}^*(-m) & m < 0 \end{cases}, \tag{10}$$

an optional multiplying term α allows to normalize the signal's strength before the correlation to account for decay in the signal over longer separation distances; a small separation is therefore preferable for highest correlation. For very small separations and using all of the time history one sets $\alpha = \beta(t) = 1$ and recovers the time averaged spatially varying convection velocity which means that the convection velocity can easily be a function of space and/or time, i.e., $U_c = U_c(\vec{y}, t)$. Also, it can be computed during run time or in a post-processing routine. Obtaining the convection velocity via correlation as opposed to from the time-averaged flow-field ensures its application to non-stationary problems and situations such as gusting inflow and curved bounding surfaces.

B. Application to potential vortex

The proposed correction is analytically evaluated for the case of an inviscid, incompressible potential vortex initially centered at $(y_1, y_2) = (0, 0)$ superimposed on a uniform background velocity U_c. The speed of sound is fixed at 340 m/s and the Mach number is chosen to be $M = 0.1$ which implies $U_c = 34$ m/s. The circulation of the vortex is chosen to be $\Gamma = \pi U_c/100$ to ensure small perturbation. The velocity potential is

$$\begin{aligned} \phi(y, \tau) &= U_c\, x - \frac{\Gamma\theta}{2\pi} \\ \theta &= tan^{-1}(\tilde{y_2}/\tilde{y_1}) \\ \tilde{y_1} &= y_1 - U_c\tau \\ \tilde{y_2} &= y_2. \end{aligned}$$

The velocities are derived from the potential and the pressure is calculated from the nonlinear unsteady Bernoulli equation as

$$\begin{aligned} u(y, \tau) &= U_c + \frac{\Gamma}{2\pi r}\sin(\theta) \\ v(y, \tau) &= \frac{-\Gamma}{2\pi r}\cos(\theta) \\ p(y, \tau) &= p_0 - \frac{\rho\Gamma^2}{8\pi^2 r^2}, \end{aligned}$$

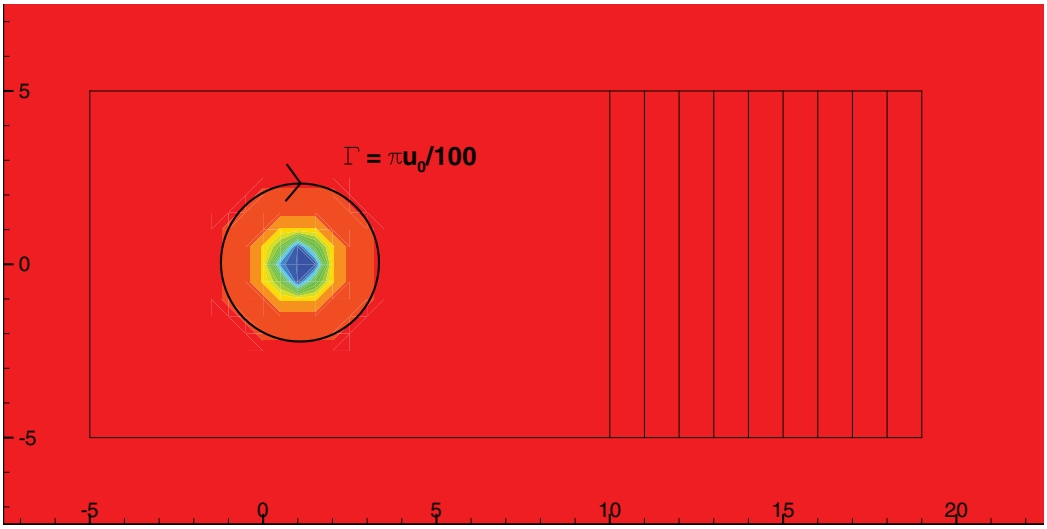

FIG. 3. The center of the vortex is visualized with the pressure field along with the Ffowcs–Williams and Hawkings planes and exit surfaces.

where r and θ are measured with respect to the center of the moving vortex. Given that the background pressure is $p_0 = p_\infty - \rho_0 U_c^2/2$, note that the unsteady Bernoulli term cancels with the cross velocity term leading to the given pressure. The microphone location is at 75D downstream since assumptions of compactness and symmetry result in no variation with respect to y in the predicted acoustic pressure. Ten exit planes are used to correlate and provide correction for surfaces terms as shown in Figure 3. The incompressibility of the flow-field means that the monopole term is zero clearly shown in Eq. (5) since the time rate of change of the integral of the mass flux is zero.

This setup demonstrates the canonical problem that the end cap methodology is designed to solve, and provides a good test because there is no time varying acoustic pressure; $p_{ac}(x,t) = p_\infty - \rho_0 \left(\frac{\partial \phi}{\partial \tau} + U_c \frac{\partial \phi}{\partial x_1}\right) = p_\infty - \rho_0 U_c^2 \rightarrow p'_{ac} = 0$. The acoustic pressure is the linear solution to the governing wave equation. Therefore, any signal from the surfaces or volumes are erroneous and must be balanced by the correction. Here the momentum flux in the dipole term in Eq. (5) becomes the largest source with the passage of the vortex core. This is balanced by the creation of volume noise as the vortex completes its passage. This is expected since the volume term is related to the surface term for a fixed surface in the convected frame of reference as

$$T_{ij} = L_{ij} - \rho u_i U_{cj} - c_0^2(\rho - \rho_0)\delta_{ij}.$$

Assuming $\rho = \rho_0$ leads to time derivatives as

$$\dot{T_{ij}} = \dot{L_{ij}} - \rho \frac{\partial u_i}{\partial \tau} U_{cj}$$

$$\ddot{T_{ij}} = \frac{\partial}{\partial \tau} \dot{L_{ij}} - \rho \frac{\partial^2 u_i}{\partial \tau^2} U_{cj}.$$

Therefore, the volume term is the time rate of change of the surface term subtracted by the second derivative of the fluctuating velocity multiplied by a mean background velocity. Furthermore, since the volume noise production in ΔV is often negligible, only the passage of the vortex into and out of the volume domain becomes important, to avoid truncation errors. This interpretation therefore demonstrates how convective sources of truncation error from surface terms are related to the corrected volume terms. In the simplified case of the convected vortex, the monopole term is zero because of incompressibility and the integrals of the derivatives of u-velocity are zero because of

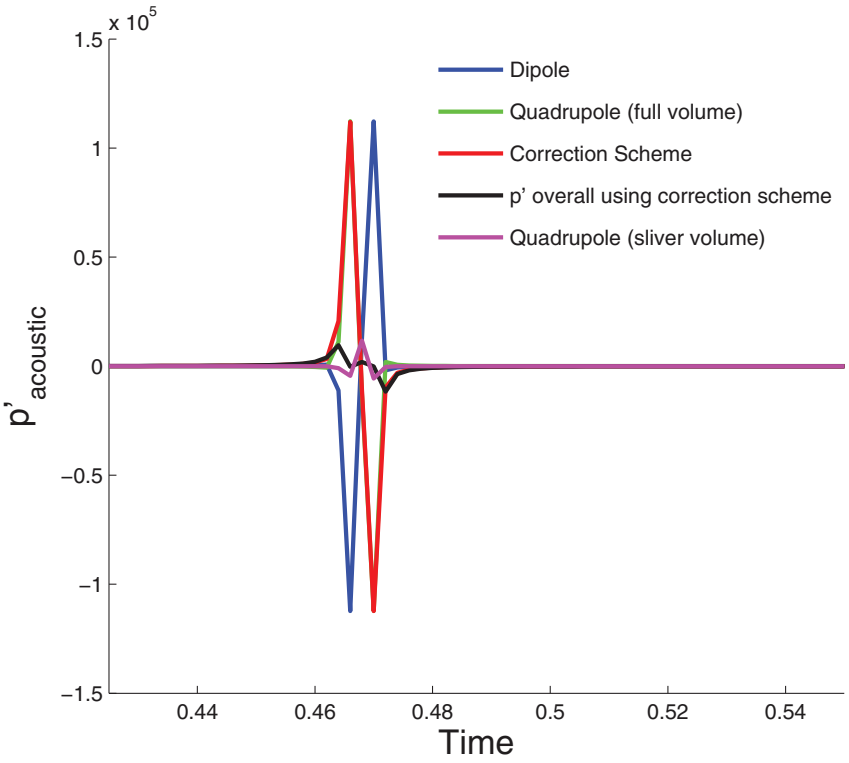

FIG. 4. The acoustic pressure for the vortex problem obtained from the FW–H equations demonstrate how the corrected volume term removes spurious noise components. The microphone location is 75D downstream. The methods compared include the method discussed as well as a FW–H approach where an extended volume computational region extends far downstream of the data surface.

symmetry which leads to the expression,

$$\begin{aligned} p'_{All} &= \frac{1}{c_0 R^*}\int_S \dot{L_{ij}} n_j \mathrm{dS} + \frac{M_0}{c_0 R^*}\int_{S_{ext}} \dot{T_{ij}} n_j \mathrm{dS} + \frac{1}{c_0^2 R^*}\int_V \ddot{T_{ij}} \mathrm{d}^3\mathrm{y} \\ &= \frac{1}{c_0 R^*}\int_S \dot{L_{ij}} n_j \mathrm{dS} + \frac{M_0}{c_0 R^*}\int_{S_{ext}} \dot{L_{ij}} n_j \mathrm{dS} + \frac{1}{c_0^2 R^*}\int_V \ddot{T_{ij}} \mathrm{d}^3\mathrm{y} \\ &= \frac{1+M_0}{c_0 R^*}\int_S \dot{L_{ij}} n_j \mathrm{dS} + \frac{1}{c_0^2 R^*}\int_V \ddot{L_{ij}} \mathrm{d}^3\mathrm{y}. \end{aligned}$$

This equation assumes a directly downstream microphone location and that the exit surface of the infinitesimal volume is near the FW−H data surface. Mitigation of the error is accomplished as a result of a convective derivative type term of the surface forces being offset by the volume term. This is the mechanism which corrects convective type truncation errors when handled completely. This is shown in Figure 4 where the surface and corrected volume terms are shown as a function of time; note their cancellation.

To examine this effect, the various terms in the FW–H equations are computed analytically in the moving frame of reference using the convected Greens function similar to Ref. 8. The convected wave form of the FW–H equations and the modified Greens function are

$$\diamond^2 = \frac{1}{c_0^2}\frac{\partial^2}{\partial t^2} - \frac{\partial^2}{\partial x_j \partial x_j} + \frac{2M_{0j}}{c_0}\frac{\partial^2}{\partial t \partial x_j} + M_{0i}M_{0j}\frac{\partial^2}{\partial x_i \partial x_j}, \tag{11}$$

$$\diamond^2[H(f)p'] = \left(\frac{\partial}{\partial t} + U_{cj}\frac{\partial}{\partial x_j}\right)[Q_k n_k \delta(f)] - \frac{\partial}{\partial x_i}[L_{ij} n_j \delta(f)] + \frac{\partial^2}{\partial x_i \partial x_j}[H(f)T_{ij}], \tag{12}$$

$$G(\mathbf{x}, \mathbf{y}, t-\tau) = \frac{1}{4\pi R^*}\delta\left(t-\tau-\frac{R}{c_0}\right), \tag{13}$$

where the distance metrics for the convected wave case are

$$R = \frac{1}{\beta^2}(R^* - M_0(x_1 - y_1))$$

$$R^* = \sqrt{(x_1-y_1)^2 + \beta^2[(x_2-y_2)^2 + (x_3-y_3)^2]}$$

$$\beta^2 = 1 - M_0^2,$$

which means

$$\widetilde{R}_i = \frac{\partial R}{\partial x_i} \Rightarrow \widetilde{R}_1 = \frac{1}{\beta^2}(\widetilde{R}_1^* - M_0),\ \widetilde{R}_2 = \frac{(x_2-y_2)}{R^*},\ \widetilde{R}_3 = \frac{(x_3-y_3)}{R^*}$$

$$\widetilde{R}_i^* = \frac{\partial R^*}{\partial x_i} \Rightarrow \widetilde{R}_1^* = \frac{(x_1-y_1)}{R^*},\ \widetilde{R}_2^* = \beta^2\frac{(x_2-y_2)}{R^*},\ \widetilde{R}_3^* = \beta^2\frac{(x_3-y_3)}{R^*}.$$

The time derivatives are brought into the integrand, as the Leibnitz terms vanish and the chain rule is applied to the FW–H equations. Compatible results were obtained by either the approach of retaining the exterior derivatives or moving them into the integrand. In the chosen wind tunnel frame of reference, the source, observer, and data surface do not move as a function of time which means $v_i = 0$ and any dot products of normals or distance metrics are also zero which simplifies the equations. Also the mean background velocity is fixed and expressed by $U_c = 34$ m/s. The FW–H equations, expressed in the wind tunnel frame, have the thickness, $p'_T = 0$ because of incompressibility, loading, p'_L, quadrupole, p'_Q, and correction, $p'_{Q_{cor}}$, terms as

$$4\pi p'_L = \int_S \left[\frac{\widetilde{R}_i}{c_0 R^*}\dot{L_{ij}}\right]\mathrm{dS},\ \ 4\pi p'_Q = \int\left[\frac{\widetilde{R}_i\widetilde{R}_j}{c_0^2 R^*}\ddot{T_{ij}}\right]\mathrm{d^3y},\ \ 4\pi p'_{Qcor} = \int_{S_{ext}}\left[\frac{M\widetilde{R}_i\widetilde{R}_j}{c_0 R^*}\dot{T_{ij}}\right]\mathrm{dS},$$

where

$$\dot{L_{ij}} = \rho\frac{\partial u_i}{\partial\tau}\left(u_j + U_{cj}\right) + \rho u_i\frac{\partial u_j}{\partial\tau} + \frac{\partial p}{\partial\tau}\delta_{ij}$$

$$\ddot{T_{ij}} = \rho\left(\frac{\partial^2 u_i}{\partial\tau^2}u_j + 2\frac{\partial u_i}{\partial\tau}\frac{\partial u_j}{\partial\tau} + u_i\frac{\partial^2 u_j}{\partial\tau^2}\right) + \frac{\partial^2 p}{\partial\tau^2}\delta_{ij}.$$

Recall that $U_{c1} = U_c$ and $U_{c2} = 0$. This means that given the derivatives of the field variables gives the complete FW–H equations for this case. They are

$$\frac{\partial u}{\partial\tau} = \frac{\Gamma U_c}{2\pi r^2}\sin(2\theta),\quad \frac{\partial v}{\partial\tau} = \frac{-\Gamma U_c}{2\pi r^2}\cos(2\theta),\quad \frac{\partial p}{\partial\tau} = \frac{-\rho\Gamma^2 U_c}{4\pi^2 r^3}\cos(\theta)$$

$$\frac{\partial^2 u}{\partial\tau^2} = \frac{\Gamma U_c^2}{\pi r^3}\sin(3\theta),\quad \frac{\partial^2 v}{\partial\tau^2} = -\frac{\Gamma U_c^2}{\pi r^3}\cos(3\theta),\quad \frac{\partial^2 p}{\partial\tau^2} = \frac{\rho\Gamma^2 U_c^2}{4\pi^2 r^4}(1-4\cos^2(\theta)),$$

which when plugged into the equations for the stress fields simplifies to

$$4\pi p'_{All} = 4\pi\left(p'_L + p'_Q + p'_{Q_{cor}}\right),$$

where

$$p'_L = \int_S \Big[\frac{\rho M\Gamma}{2\pi r^2 R^*}\Big\{\widetilde{R}_1(U_c\sin(2\theta)n_x - \frac{\Gamma}{2\pi r}(\cos(3\theta)n_x + \sin(3\theta)n_y)) + \widetilde{R}_2(-U_c\cos(2\theta)n_x - \frac{\Gamma}{2\pi r}(\sin(3\theta)n_x - \cos(3\theta)n_y))\Big\}\Big]_{ret} \mathrm{dS}$$

$$p'_Q = \int_V \Big[\frac{3\rho M^2\Gamma^2}{4\pi^2 r^4 R^*}(-\widetilde{R}_1\widetilde{R}_1\cos(4\theta) - 2\widetilde{R}_1\widetilde{R}_2\sin(4\theta) + \widetilde{R}_2\widetilde{R}_2\cos(4\theta))\Big]_{ret} \mathrm{d^3y}$$

$$p'_{Q_{cor}} = \int_{S_{ext}} \Big[\frac{\rho M^2\Gamma^2}{4\pi^2 r^3 R^*}(-\widetilde{R}_1\widetilde{R}_1\cos(3\theta) - 2\widetilde{R}_1\widetilde{R}_2\sin(3\theta) + \widetilde{R}_2\widetilde{R}_2\cos(3\theta))\Big]_{ret} \mathrm{dS}.$$

Note the cancellation for the simplified cases of having extrusion surfaces aligned in principle directions. For example in the x-direction,

$$p'_L = \frac{-\rho M\Gamma^2}{4\pi^2 R^*}\Big(\int_{S,front/back}\Big[\frac{\cos(3\theta)n_x}{r^3}\Big]\mathrm{dS} + \int_{S,top/bottom}\Big[\frac{\sin(3\theta)n_y}{r^3}\Big]\mathrm{dS}\Big)$$

$$p'_Q = \frac{-3\rho M^2\Gamma^2}{4\pi^2 R^*}\int_V\Big[\frac{\cos(4\theta)}{r^4}\Big]\mathrm{d^3y}$$

$$p'_{Q_{cor}} = \frac{-\rho M^2\Gamma^2}{4\pi^2 R^*}\int_{S_{ext}}\Big[\frac{\cos(3\theta)}{r^3}\Big]\mathrm{dS}.$$

Hence under assumptions of compactness

$$p'_{All} = -\frac{\rho M\Gamma^2}{4\pi^2 R^*}\Big(\int_{S,front}\Big[-\frac{\cos(3\theta)}{r^3}\Big]\mathrm{dS} + \int_{S,back}\Big[(1+M)\frac{\cos(3\theta)}{r^3}\Big]\mathrm{dS} + \int_{S,top/bottom}\Big[\frac{\sin(3\theta)n_y}{r^3}\Big]\mathrm{dS} + 3M\int_V\Big[\frac{\cos(4\theta)}{r^4}\Big]\mathrm{d^3y}\Big). \quad (14)$$

Equation (14) is numerically integrated at various emission times. The recovered noise from the FW–H equations for this flow field is approximately zero, decays quickly away from the vortex

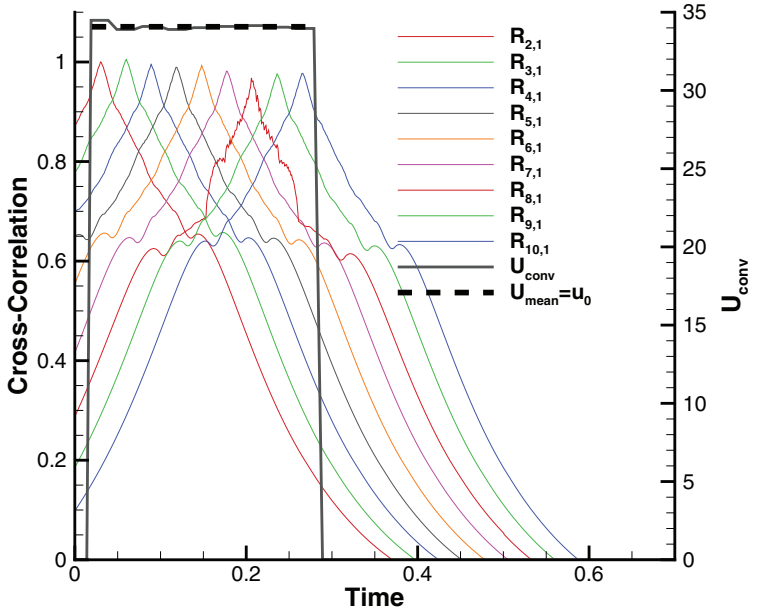

FIG. 5. The cross-correlation coefficients between each plane with respect to the first plane are shown as well as the convection velocity derived from the method. The mean of the intervals is $U_c = M * c0 = 34.0$ as specified and is also plotted.

center, and exhibits the $(1 + M)$ behavior in the surface terms as expected. It is important to note that it is only after the inclusion of the quadrupole correction terms that the cancellation becomes effectively complete. This indicates that the inclusion of the quadrupole term is necessary for the correct changeover of terms as well as the the application of the exit flux correction.

Finally, we demonstrate the ability of the proposed cross-correlation approach to account for a time-varying convection velocity by windowing our correlation function. We choose a top-hat filter of length ten time spaces to ensure smoothness in results based on the chosen dx, U_c, and dt. The resulting cross-correlation coefficients are plotted as a function of time along with the resulting convection velocity as shown in Figure 5. This clearly demonstrates the ability to handle time varying convection velocities.

III. NUMERICAL METHOD

We apply the proposed methodology to compute the sound from the flow over circular cylinders at Reynolds numbers of 150, 10 000, and 89 000. The $Re = 150$ cylinder flow is computed using DNS of the compressible Navier–Stokes equations, while the higher Reynolds number flows are simulated using LES of the incompressible Navier–Stokes equations. Both simulations use unstructured grids.

The unstructured grid, finite-volume algorithm for solving the incompressible Navier–Stokes equations is that developed by Ref. 15. The algorithm emphasizes discrete-kinetic energy conservation in the inviscid limit which enables it to simulate high-Reynolds number flows in complex geometries without adding numerical dissipation. The solution is advanced using a predictor-corrector methodology where the velocities are first predicted using the momentum equation alone, and then corrected using the pressure gradient obtained from the Poisson equation yielded by the continuity equation. The time advancement is implicit and uses the Crank–Nicholson discretization with a linearization of the convection terms. The algorithm has been validated for a wide range of complex problems which include a gas turbine combustor geometry,[15] predicting propeller crashback,[16,17] and turbulent jets.[18–21] The LES subgrid stresses in the present simulations are performed using a dynamic Lagrangian model where the Lagrangian time scale is dynamically computed as proposed by Park and Mahesh[22] and Verma *et al.*[16]

The compressible equations are solved using an algorithm developed for unstructured grids by Ref. 22. The algorithm employs a least-square method for flux reconstruction on faces of control volumes, viscous flux splitting to ensure that the dominant component only depends on the nearest neighbors and is therefore more accurate at high wavenumbers, and devoid of odd-even decoupling. The algorithm uses a shock-capturing scheme that was originally proposed by Ref. 23 for structured meshes and was extended by Ref. 22 to unstructured meshes, and further localized to reduce

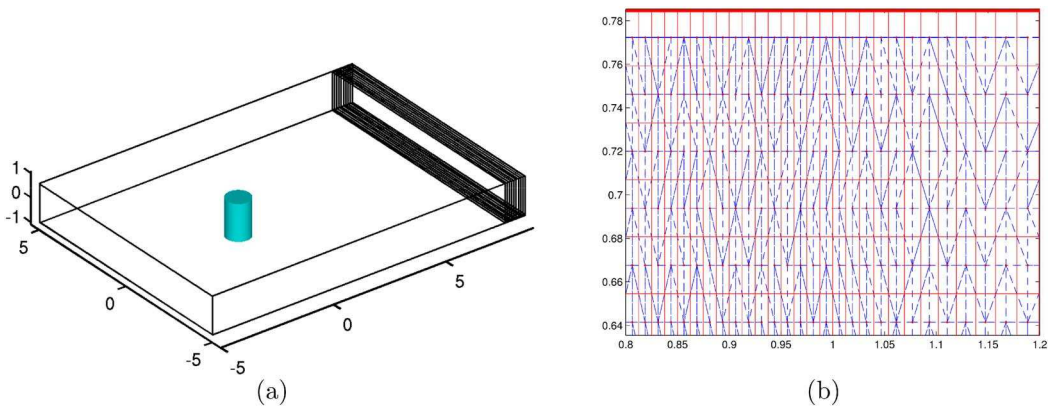

FIG. 6. The geometric extraction of the planes for the Re = 10k cylinder are demonstrated in (a) and a closeup of the top plane in (b) shows the Voronoi areas (squares), Delaunay triangulation (triangles), and the boundary (bold-top) of the projected surface elements. Note the contraction of grid spacing with increasing x-distance demonstrating the correspondence between the FW−H data surface and the computational grid.

unnecessary numerical dissipation. Time advancement is explicit and uses the second order Adams Bashforth method. The methodology has also been shown to perform well in various complex flows such as supersonic boundary layer transition due to roughness element[24] and distributed roughness,[25] and LES of decaying isotropic turbulence and shock/turbulence interaction.[26]

The FW–H surfaces are prescribed on background unstructured grids, which makes arbitrary surface extraction within the computational domain challenging. We define arbitrary surfaces and discretize the surface in a manner that reflects the volume grid in the interior. We accomplish this by projecting the centroids of the volume grid on the FW−H surface and then generate a constrained Delaunay triangulation for the connectivity, while its mesh dual, the Voronoi diagram capped by the boundary, provides the projected face areas. Finally, we establish exterior and interior volumes which allow for surface integration to be handled in tandem with consistent volume integration. Alternatively, all faces which intersect the desired surface could be used to represent the surface, but discontinuous normals, large numbers of faces, and highly discontinuous volume representations present their own unique challenges. The chosen spatial decomposition ensures that a projected partner separated by a determinable distance exists between any two extraction stations. An example of the extraction technique is shown in Figure 6.

IV. RESULTS

We evaluate the proposed FW−H implementation including quadrupole terms by computing the sound emitted by flow over a circular cylinder at Reynolds number of 150, 10 000, and 89 000, respectively.

A. Re = 150 cylinder flow

The acoustics of low Reynolds' number cylinder flow have been studied by several investigators, e.g., Refs. 27–30; also simplified models have been developed, which render this a good validation problem. Subtle differences in reported results mostly arise from the choice of Greens' function and Doppler shifts but appropriate comparisons can still be made. Phillips constructed a simplified model for Aeolian tones for cylinders and experimented with a $d = 0.0123$ cm cylinder over $110 < Re < 160$. For short spans, b, and in-plane observers at distance R and radiation angle θ, Phillips model, with model constant κ, predicts acoustic power $\bar{I}$ given the Strouhal number, St, and flow conditions ρ, V_0, c, and M as

$$\bar{I} = \frac{\kappa^2 St^2 b^2 \rho_0 V_0^6 \sin^2\theta}{32 c_0^3 R_0^2 (1 - M\cos\theta)^4}. \tag{15}$$

Inoue performed computations of a $Re = 150$ cylinder and reported on how Doppler shift is important in the calculation of the two-dimensional acoustic field and how acoustic pressure decays in this configuration. We use a two-dimensional Greens' function to compare to Inoue.

We perform a compressible DNS of the flow around a two-dimensional circular cylinder at $M = 0.2$ and $Re = 150$ with the described FW−H acoustic analogy to recover the noise at a distance of 75 and 100D. The compressible results, with an exit sponge, allow for a direct calculation of the noise in the far-field and serves as the basis of comparison for the different methodologies discussed previously. The flow field (lift, drag, and basal pressure coefficient) is in good agreement with Inoue,[28] Beaudan and Moin,[31] and Norberg,[32] i.e., Table I. The Strouhal number agrees with the scaling proposed by Fey, Konig, and Eckelmann[33] of $St = 0.2684 - 1.0356Re^{-0.5} = 0.1648$. The sound comparisons are similarly good. For the sound pressure level (SPL) at a Doppler shifted direction of $\theta = \pi/2$ at $r = 100\,D$, the Phillips model predicts 87.6 dB ± 6.02 dB based on Phillips' suggested range of $0.5 < k < 2$. Inoue reports a maximum value of 88.5 dB and our DNS recovers 89.0 dB, all in close agreement. We compare the time histories of the received pressure at this location against Inoue and obtain good agreement as shown in Figure 7. Also, based on Inoue's scaling arguments for preferential radiation direction $\theta_p = \cos^{-1}(M)$ we predict 81° which compares well to the predicted maximum of 81.4°. These results show that our DNS accurately captures both the flow field and the acoustic field.

TABLE I. Summary of surface forces and frequencies.

Metric	Result	Norberg
$C_{L,\,press,\,max}$	0.2540	0.28
$C_{L,visc,max}$	0.0428	0.045
$C_{D,\,press,\,max}$	0.9824	1.00
$C_{D,visc,max}$	0.4046	0.34
$St\,C_L$	0.1646	0.1652
$St\,C_D$	0.3292	0.3304

Our proposed FW−H methodology is used to compute the far-field sound and is compared to DNS at 180 microphone locations at 75D from the cylinder. The data are aggregated via a 2-D FW−H implementation that has a porous surface located as fixed planes 5D in front and to the top and bottom of the cylinder. A series of ten exit surfaces are constructed from $x = 5D$ to $7.25D$ downstream of the cylinder. Figure 8 evaluates the proposed end cap correction. Note how the correction scheme reduces the maximum value of SPL from 120 dB down to 67.204 dB in Figure 8(a). As discussed by Inoue, the expected relative ratio between surface and volume terms is the Mach number, which yields an estimate of 67.574 dB. Also, note that with the correction employed the directivity takes on the characteristic quadrupole shape consistent with Gloerfelt *et al.*[34] Figure 8(b) illustrates the ability of the dynamic procedure to allow for spatial variation of the convection velocity. Here the convection velocity is assumed to vary across the width of the wake and note how this subtle change provides for diminished off angle errors in the directivity of the quadrupole terms at $f = 2f_0$. This suggests that a fixed convection velocity over-emphasizes the center of the wake in the acoustic analogy. The spatial variation slightly improves the predictions; the improvement depends on the extent of the shear in the wake.

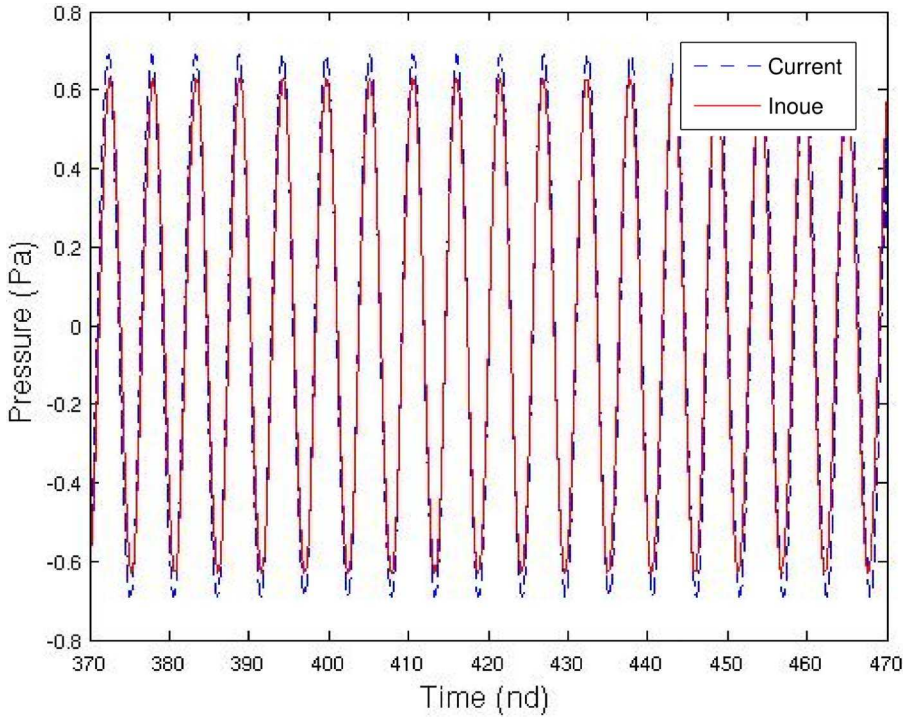

FIG. 7. For the Re = 150 cylinder, a comparison of the time histories of the surface noise is plotted versus Inoue[28] at $\theta = \pi/2$, $R = 100D$.

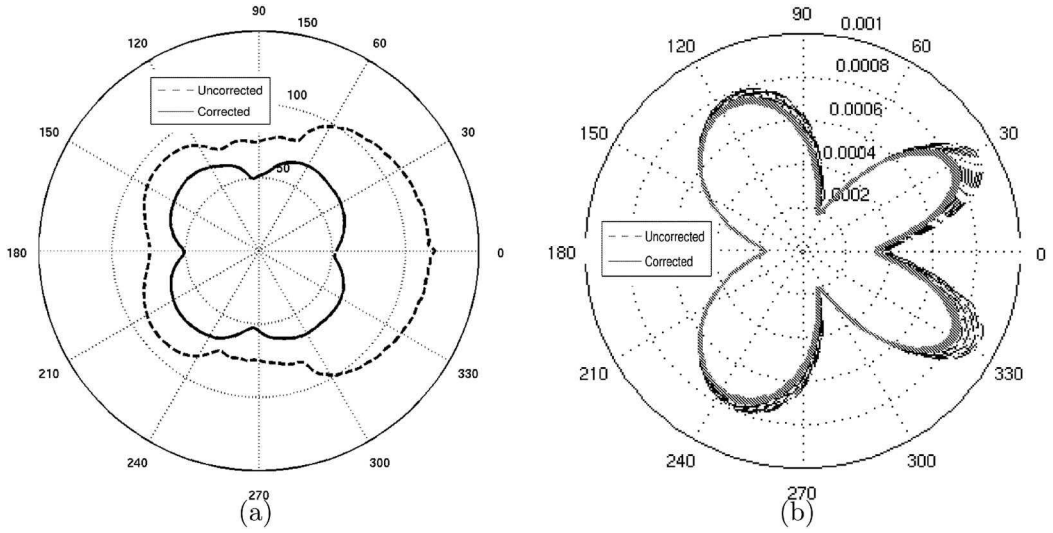

FIG. 8. Directivity and comparison of volume terms for the Re = 150 cylinder. (a) shows the comparison of the recovered quadrupole noise, in SPL(dB), using the prescribed end cap methodology compared to the noise that is computed using no closure mechanism at all. (b) compares the effect of using a fixed or spatially varying convection velocity on recovered noise in p'_{rms} directivity at a discrete frequency, $St = 0.3292$.

The sensitivity to volume size and the dynamic approach to calculate U_c are examined in Figure 9. The instantaneous far-field pressure is shown in (a) where the volume noise is calculated for ten volumes each differing by a single grid element dx in the streamwise direction. Note the scatter in the absence of correction, but when added to the correction for each volume, one recovers the corrected volume noise with less phase and amplitude shifts. Here the convection velocity is externally prescribed. The effect of dynamically computing the convection velocity is shown in (b) where the phase and amplitude variance is significantly reduced if a dynamically calculated U_c is used as opposed to a fixed value. Clearly, the phase and amplitude variation decreases across the ten

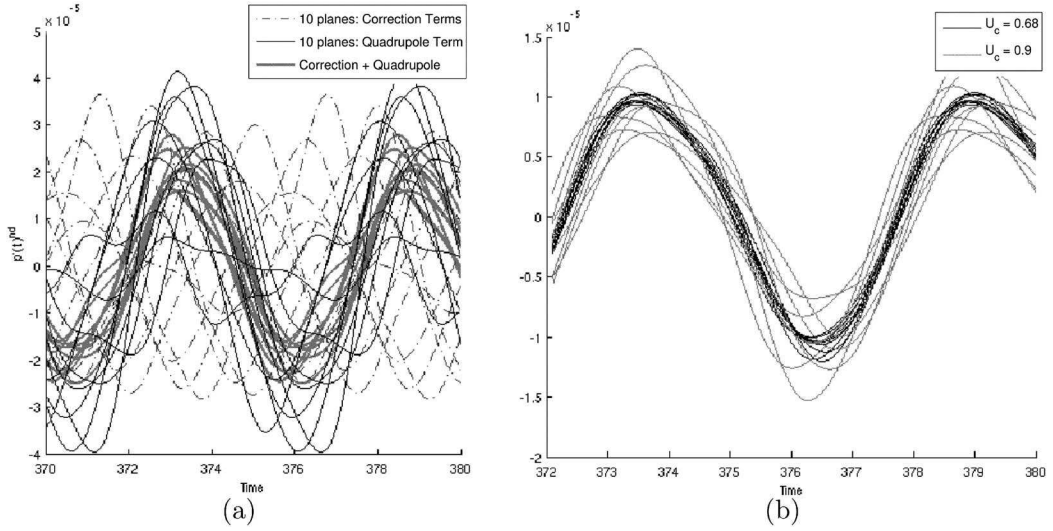

FIG. 9. The non-dimensional acoustic pressure as a function of time for Re = 150 cylinder. (a) displays the calculated volume term, the end cap correction, and the corrected volume noise with an assumed $U_c = 1.0$. (b) shows the same curve as before now with an assumed $U_c = 0.9$ and with the convection velocity obtained by correlation as $U_c = 0.68$. Note how dispersion in the resulting curves is decreased by using the cross-correlation velocity.

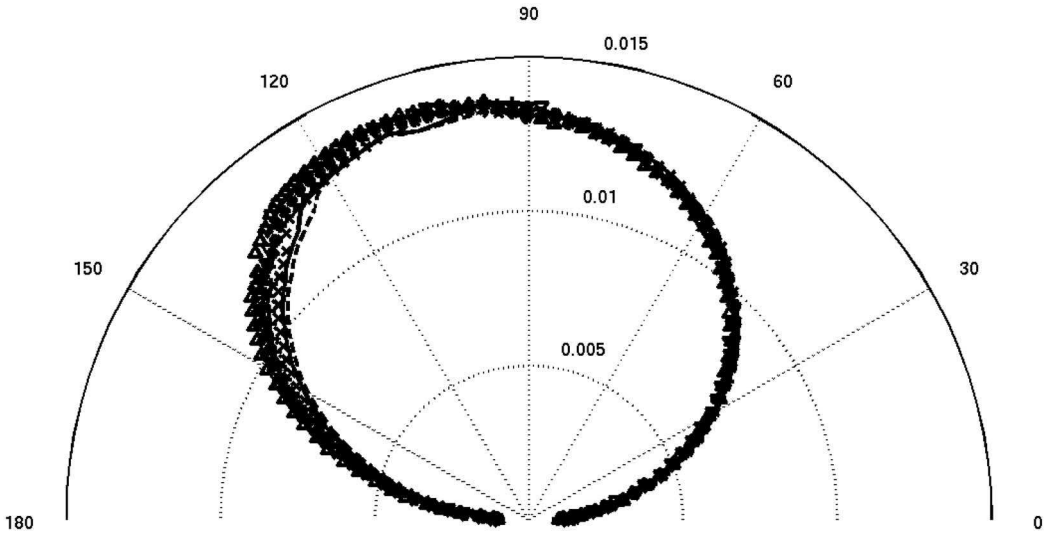

FIG. 10. Effect of end cap plane spacing and downstream location for the Re = 150 cylinder. (−) dx=1dx,L=5D; (-) dx=2dx,L=5D; (x) dx=1dx,L=10D; (◇) dx=2dx,L=10D; (+) dx=3dx,L=10D; (∗) dx=4dx,L=10D; (△) dx=1dx,L=35D; (∇) dx=2dx,L=35D.

volumes demonstrating both insensitivity to size of the end cap volumes in our proposed approach, and the importance of the convection velocity.

The sensitivity to exit plane location was tested by varying the exit plane from 5D to 35D and varying the spacing between correlated planes from dx to 4dx. Note how the results, shown in Figure 10, are insensitive to both plane location as well as inter-plane spacing.

Figure 11 compares the proposed end cap correction method to the other commonly used approaches to compute the overall SPL. Note that the proposed approach is noticeably better. A similar comparison was performed at fixed frequencies. At the Strouhal number of the lift component, $f = f_0$, the proposed method was again seen in Figure 12 to agree well with the DNS. On the other hand, large variance is seen between the phase averaged approach and others; this is because the distances between subsequent planes are quite small implying large correlation which violates the fundamental assumptions of the phase-average approach. At $f = 2f_0$ which corresponds primarily to the drag fluctuations the proposed method shows good agreement to DNS, i.e., Figure 13. In contrast, the open and phase averaged methodologies in particular show large variation from DNS data. For the open calculation, there is no predicted sound propagated in the downstream direction while the phase averaging is inaccurate for the same reasons as those described at $f = f_0$.

B. Re = 10 000 cylinder

We consider a $Re = 10\,000$ cylinder as an example of turbulent flow for which we can compare to other simulations. Khaligi *et al.*[35] developed a hybrid boundary element approach which decouples scattered sources from directly propagating sources and compared against a FW−H computation. We perform wall resolved LES with an initial standoff spacing of $\Delta n^+ = 0.52$ with a total control volume count of 54×10^6. The grid extends 20D upstream and 40D downstream and is πD long in the span.

A representative flow visualization is shown in Figure 14, for which the averaged flow field is computed and compared to those of Khalighi *et al.* in Figures 15(a) and 15(b); note the good agreement for mean streamwise velocity and fluctuating components. We surmise from this result and the surface forces in Table II that fair agreement between flow solutions exist. The results of Figure 16 show good agreement in the recovered noise power at a fixed location of (−1.2D,16.2D) indicating consistent flow fields and acoustic content. Our methodology is compared at the dominant frequencies that are displayed in Figures 17(a)–17(d). Here we find close results with the hybrid

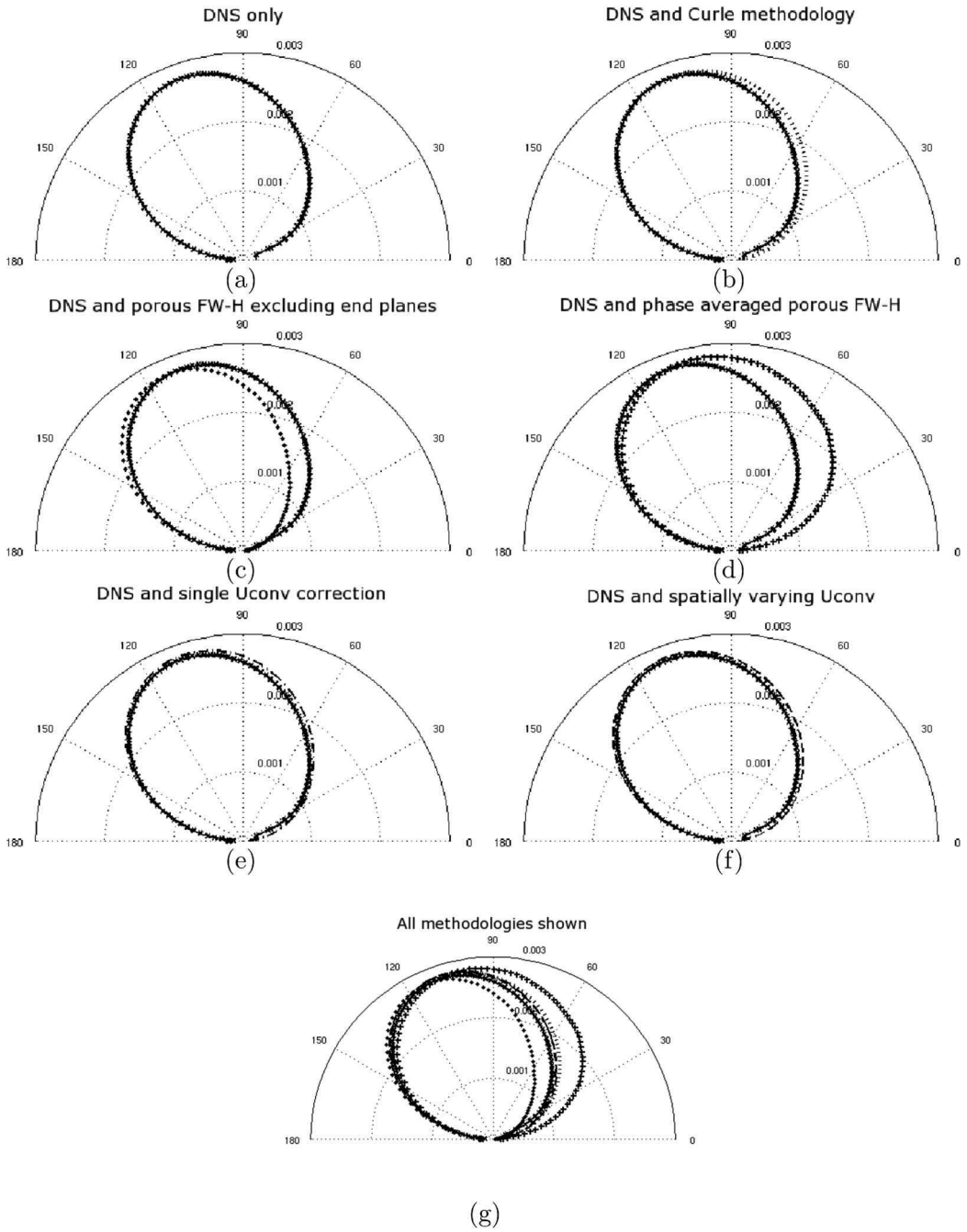

FIG. 11. Directivity of the received sound, p'_{rms}, for the Re = 150 cylinder. (a) is the directivity of received pressure fluctuations directly from the DNS at the microphone locations. (b) is the comparison of the predicted noise using a Curle methodology compared to the direct DNS approach. (c) a FW−H approach with no planes at fixed x-locations downstream of the body, i.e., and open formulation. (d) using a phase average approach over ten downstream planes as suggested by Shur *et al.*[13] (e) a FW−H approach with the described end cap methodology with a single U_{conv} applied at each of the ten exit planes and (f) the same end cap technique with a $U_{conv} = U_{conv}(y)$ approach. (g) Comparison of all of the directivities of the different methodologies as shown.

methodology which has the effect of volumetric effects through the application of scattered noise in conjunction with direct noise production external to the body. Often the discrepancies that exist are bounded by the FW−H results of Khalighi *et al.* which would demonstrate that surfaces terms are dominant and it is the variation in volume terms that produce the difference.

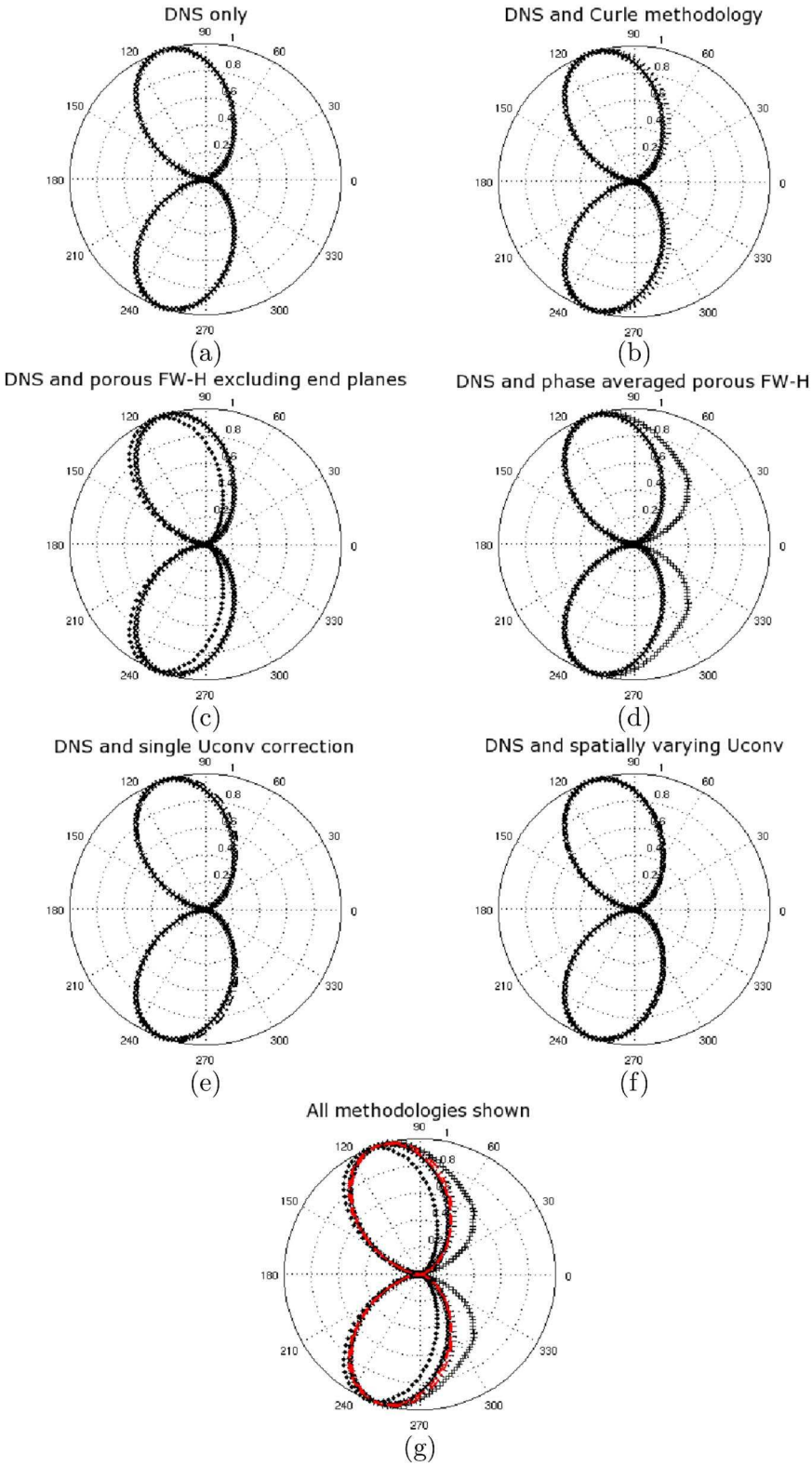

FIG. 12. Directivity of the sound for the Re = 150 cylinder at $f = f_0$ for various approaches. (a) shows DNS only. (b) has a Curle surface approach. (c) is the open exit formulation. (d) is the phase average approach over ten downstream planes. (e) is a FW−H approach with a single U_{conv}. (f) is a FW−H approach with $U_c = U_c(y)$. (g) is a comparison of all of the different methodologies.

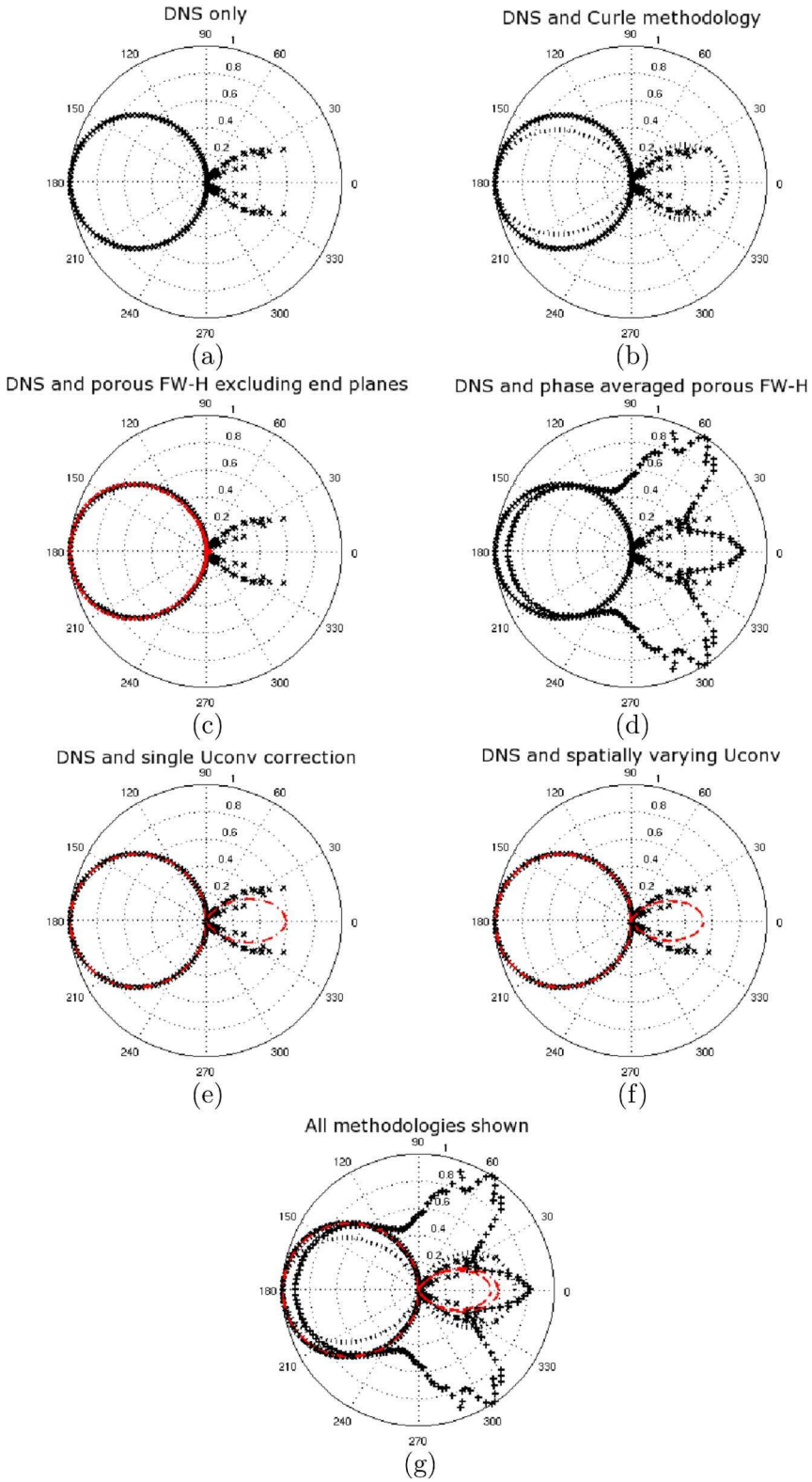

FIG. 13. Directivity of the sound for the Re = 150 cylinder at $f = 2f_0$ for various approaches. (a) shows DNS only. (b) has a Curle surface approach. (c) is the open exit formulation. (d) is the phase average approach over ten downstream planes. (e) is a FW−H approach with a single U_{conv}. (f) is a FW−H approach with $U_c = U_c(y)$. (g) is a comparison of all of the different methodologies.

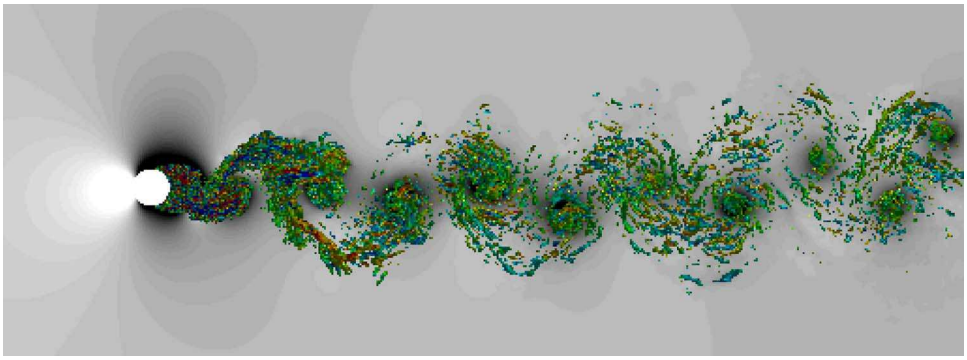

FIG. 14. A Re = 10 000 cylinder flow is visualized using an iso-surface of λ_2 colored by u-velocity with the pressure field in grey-scale.

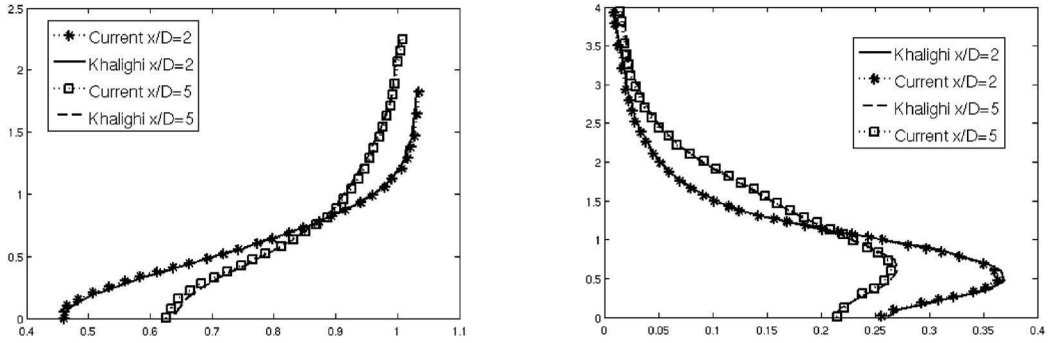

FIG. 15. For the Re = 10 000 cylinder, the parameters $\bar{u}$ (a) and u'_{rms} (b) from the average flow field at two x-locations[2,5] are compared to reported results of Khalighi *et al.*[35]

C. Re = 89 000 cylinder

The highest Reynolds' number cylinder flow that we investigate, $Re = 89\,000$, is chosen to compare against the experiments of Revell *et al.*[36] who placed a cylinder into the exhaust of a nozzle and captured the noise with a microphone array. More recently, Cox *et al.*[37] and computed this configuration using the unsteady Reynolds-averaged Navier–Stokes (URANS) approach with two different closure models, and obtained results which indicated only dominant frequencies and their harmonics. Our solution has been computed on a grid with 82×10^6 grid points with an initial spacing of $\Delta n^+ = 0.78$. The grid extends 20D upstream, above and below and 40D in the downstream direction. The span has an extent of πD with 150 points.

We can see from Figure 18 that the flow structure resembles the flow at lower Reynolds' numbers but has a larger range of scales and a larger spreading angle. The noise at $\theta = \pi/2$ and $r = 128D$ as shown in Figure 19(d) shows good agreement at the fundamental frequency as well as the drag and first lift harmonic. The first lift harmonic for the current results show some shift relative to the

TABLE II. Summary of surface forces, fluctuations, and frequencies for $Re = 10k$ cylinder.

Metric	Current	Comparison	Author
C'_L	0.503	0.506	Norberg
$\langle C_D \rangle$	1.336	1.29	Norberg/Khalighi *et al.*
C'_D	0.090	0.091	Khalighi *et al.*
$St\,C_L$	0.197	0.196	Norberg

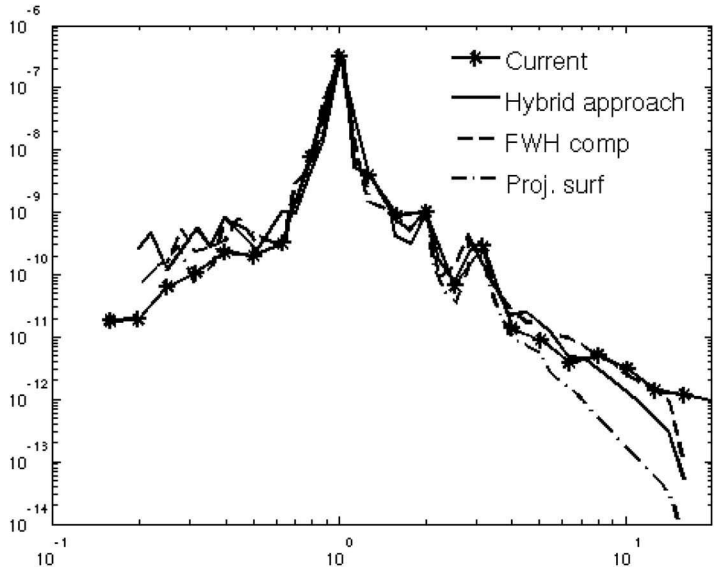

FIG. 16. A comparison of the predicted noise power versus frequency at the location (−1.2D,16.2D) for the Re = 10,000 cylinder is plotted against Khalighi *et al.*[35]

experiment but our results show the frequency at $f \approx 3f_0$ where the first overtone of lift should reside. In contrast, the URANS predicts no harmonics of lift and drag since it is a 2D computation and has a larger shift in the Strouhal frequency relative to current results. There is a discrepancy at lower frequencies but it is not due to insufficient time samples as we have 180 units of time giving spectral

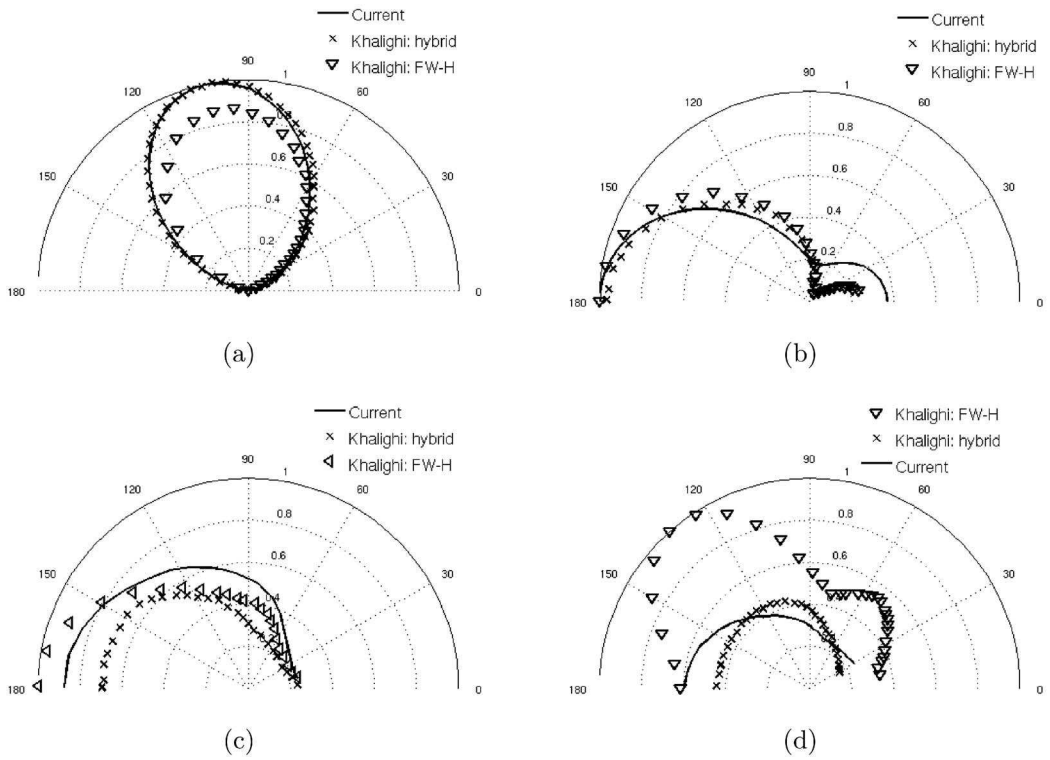

FIG. 17. A comparison of the directivities for the Re = 10 000 cylinder at select frequencies (a) $f = f_0$, (b) $f = 2f_0$, (c) $f = 4f_0$, and (d) $f = 8f_0$ for the described end cap methodology versus two methods presented by Khalighi *et al.*[35]

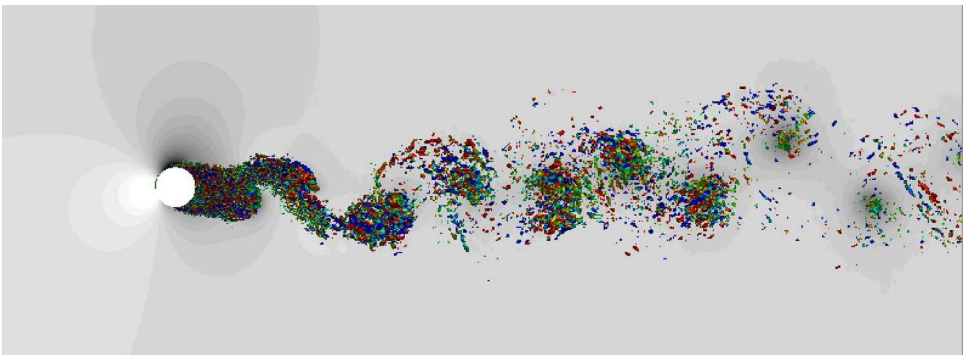

FIG. 18. The Re = 89 000 cylinder flow is visualized by λ_2 colored by u-velocity with pressure field shown in grey scale.

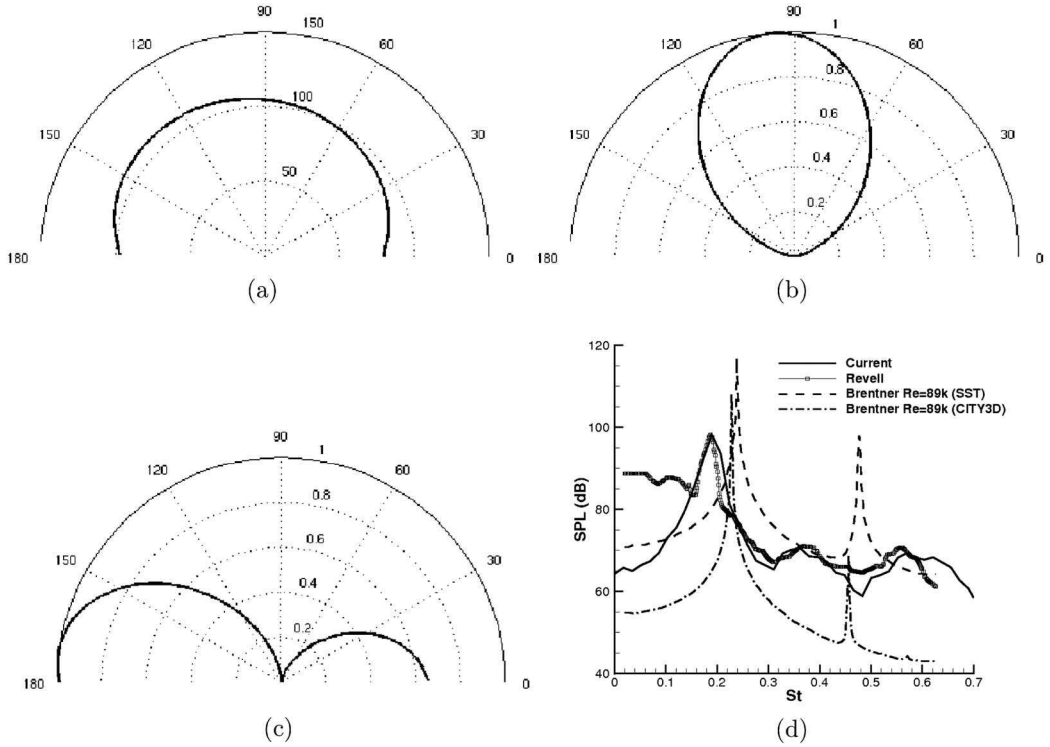

FIG. 19. The acoustic p'_{rms} directivities for the Re = 89 000 cylinder are shown for the overall and major component frequencies as (a) overall, (b) $f = f_0$, and (c) $f = 2f_0$, respectively. The frequency content of the generated noise, SPL(dB) vs frequency, at the location $\theta = \pi/2$ and L=128D is compared to the experiments of Revell *et al.*[36] and the computations of Cox and Brentner.[37]

discrimination of 0.0055. The directivities of the overall sound production is broader than that of the Re = 1e4 case, but the component harmonic directivities show similar results to those at lower Reynolds' numbers. The reason for this subtle difference is that the higher frequencies, not shown on the spectral plot, contain more of the overall content, though still quite a small relative to the dominant harmonics. Overall the agreement with experiment is quite good and significantly better than the URANS.

V. SUMMARY

A novel end cap methodology to account for volume sources or as correction to surface terms in the context of porous FW−H equations has been proposed and analyzed. This method uses

multiple exit planes to extract a convection velocity that can vary as a function of space and time which establishes a model constant for the correction term. This correction term balances the net flux of momentum traversing the porous FW−H planes that exists in the dipole term or if using a Curle surface provides the missing component of the volume term exterior to the bounding volume. This approach allows for using the more sensitive FW−H equations in integral form and allows for efficient computation of the acoustic sources due to the ability to maintain minimal volumes while providing the ability to query noise contributions from specific volume regions. The proposed methodology works best over short intervals where surface conditions are representative of frozen vortices which are highly correlative. This method is in contrast to the approach of Shur *et al.*[13] where numerous planes at large separation distances help provide largely phase independent results which are phase averaged to remove spurious noise.

The feasibility of this end cap correction approach was validated for the case of a potential vortex and then was used to predict the noise from various Reynolds' number cylinder flows. The potential flow case demonstrated the terms which are balanced between the dipole noise and the correction term. This case also demonstrated the ability to have a convection velocity that varies as a function of time based on an averaging scheme. For the low Reynolds' number cylinder flow we evaluated the noise computations against Inoue and the model of Phillips with close agreement. We also compared our results to other proposed closure methods and found better agreement with respect to the DNS. The approach with spatially varying convection velocity in the correction term gave the best results. We examined the effect of porous plane placement and displacement and found little sensitivity to these parameters. These results indicate very good accuracy with low computational cost validating the attractiveness of the approach.

The method was then extended to highly three-dimensional flows for cylinders at $Re = 10\,000$ and 89 000. For both of these cases, flow comparisons with previous work show good agreement in the resolved sound fields. The method therefore shows good extension to highly turbulent external flows. Furthermore, the predictive ability with high resolution LES demonstrated significantly better results than U-RANS when compared against experiment for the highest Reynolds number case. The larger range of scales and the inherent three-dimensionality do not require the assumed correlation length approach of the two dimensional U-RANS and is reflected in the noise results with more frequency content represented. Overall, the proposed approach has attractive features such as small but customizable volume computation and higher accuracy than other standard methods, that warrant further application and investigation.

ACKNOWLEDGMENTS

This work was supported by the United States Office of Naval Research (ONR) under Grant No. N00014-14-1-0304 with Dr. Ki-Han Kim as technical monitor. Computing resources were provided by the DoD HPCMP Open Research Systems, the Minnesota Supercomputing Institute, and in part by the National Science Foundation through XSEDE resources provided by the XSEDE Science Gateways program.

[1] M. J. Lighthill, "On sound generated aerodynamically. Part I. General theory," Proc. R. Soc. London A **211**, 564–587 (1952).
[2] N. Curle, "The influence of solid boundaries upon aerodynmical sound," Proc. R. Soc. London A **231**, 505–514 (1955).
[3] J. E. Ffowcs-Williams and D. L. Hawkings, "Sound generation by turbulence and surfaces in arbitrary motion," Philos. Trans. R. Soc. London **264A**, 321–342 (1969).
[4] A. S. Lyrintzis, "Surface integral methods in computational aeroacousticsfrom the (cfd) near-field to the (acoustic) far-field," Int. J. Aeroacoust. **2**(2), 95–128 (2003).
[5] K. S. Brentner and F. Farassat, "An analytical comparison of the acoustic analogy and kirchhoff formulations for moving surfaces," AIAA J. **36**(8), 1379–1386 (1998).
[6] K. S. Brentner and F. Farassat, "Modeling aerodynamically generated sound of helicopter rotors," Prog. Aerosp. Sci. **39**(2–3), 83–120 (2003).
[7] D. Casalino, "An advanced time approach for acoustic analogy predictions," J. Sound Vibrat. **264**, 583–612 (2003).
[8] A. Najafi-Yazdi, G. A. Bres, and L. Mongeau, "An acoustic analogy formulation for moving sources in uniformly moving media," Proc. R. Soc. A **467**(2125), 144–165 (2010).
[9] F. Farassat, "Theory of noise generation from moving bodies with an application to helicopter rotors," Langley Research Center, Hampton, VA, NASA Technical Report R-451, 1975.

[10] M. S. Howe, *Theory of Vortex Sound* (Cambridge University Press, Cambridge, 2003).
[11] M. E. Goldstein, *Aeroacoustics* (McGraw-Hill, New York, 1976).
[12] J. E. Ffowcs Williams, "Sound sources in aerodynamics–fact and fiction," AIAA J. **20**(3), 307–315 (1982).
[13] M. L. Shur, P. R. Spalart, and M. K. Strelets, "Noise prediction for increasingly complex jets. Part I. Methods and Tests," Intl. J. Aeroacoust. **4**(3–4), 213–246 (2005).
[14] M. Wang, S. K. Lele, and P. Moin, "Computation of quadrupole noise using acoustic analogy," AIAA J. **34**(11), 2247–2254 (1996).
[15] K. Mahesh, G. Constantinescu, and P. Moin, "A numerical method for large-eddy simulation in complex geometries," J. Comput. Phys. **197**(1), 215 (2004).
[16] A. Verma, H. Jang, and K. Mahesh, "The effect of an upstream hull on a propeller in reverse rotation," J. Fluid Mech. **704**, 61–88 (2012).
[17] A. Jang and K. Mahesh, "Large eddy simulation of flow around a reverse rotating propeller," J. Fluid Mech. **729**, 151–179 (2013).
[18] C. Babu and K. Mahesh, "Upstream entrainment in numerical simulations of spatially evolving round jets," Phys. Fluids **16**(10), 3699–3705 (2004).
[19] S. Muppidi and K. Mahesh, "Study of trajectories of jets in cross-flow using direct numerical simulations," J. Fluid Mech. **530**, 81–100 (2005).
[20] S. Muppidi and K. Mahesh, "Direct numerical simulation of round turbulent jets in crossflow," J. Fluid Mech. **574**, 449–461 (2007).
[21] S. Muppidi and K. Mahesh, "Direct numerical simulation of passive scalar transport in transverse jets," J. Fluid Mech. **598**, 335–360 (2008).
[22] N. Park and K. Mahesh, "Numerical and modeling issues in les of compressible turbulent flows on unstructred grids," AIAA Paper No. 2007-722, 2007.
[23] H. C. Yee, N. D. Sandham, and M. J. Djomehri, "Low-dissipative high-order shock-capturing methods using characteristic-based filters," J. Comput. Phys. **150**(1), 199–238 (1999).
[24] P. Iyer, S. Muppidi, and K. Mahesh, "Boundary layer transition in high-speed flows due to roughness," AIAA Paper No. 2012-1106, 2012.
[25] S. Muppidi and K. Mahesh, "DNS of roughness-induced transition in supersonic boundary layers," J. Fluid Mech. **693**, 28–56 (2012).
[26] X. Chai and K. Mahesh, "Dynamic-equation model for large-eddy simulation of compressible flows," J. Fluid Mech. **699**, 385–413 (2012).
[27] O. M. Phillips, "The intensity of aeolian tones," J. Fluid Mech. **1**, 607–624 (1956).
[28] O. Inoue and N. Hatakeyama, "Sound generation by a two-dimensional circular cylinder in uniform flow," J. Fluid Mech. **471**, 285–318 (2002).
[29] C. Cheong, P. Joseph, Y. Park, and S. Lee, "Computation of aeolian tone from a circular cylinder using source models," Appl. Acoust. **69**(2), 110–126 (2008).
[30] D. P. Lockard, "An efficient, two-dimensional implementation of the Ffowcs Williams and Hawkings equation," J. Sound Vibrat. **229**(4), 897–911 (2000).
[31] P. Beaudan and P. Moin, "Numerical experiments on the flow past a circular cylinder at sub-critical Reynolds number," Thermosciences Division, Department of Mechanical Engineering TF-62, Stanford University, 1994.
[32] C. Norberg, "Fluctuating lift on a circular cylinder: review and new measurements," J. Fluids Struct **17**(1), 57–96 (2003).
[33] U. Fey, M. König, and H. Eckelmann, "A new StrouhalReynolds-number relationship for the circular cylinder in the range $47 < re < 105$," Phys. Fluids **10**, 1547–1549 (1998).
[34] X. Gloerfelt, F. Perot, C. Bailly, and D. Juve, "Flow-induced cylinder noise formulated as a diffraction problem for low mach numbers," J. Sound Vibrat. **287**, 129–151 (2005).
[35] Y. Khalighi, A. Mani, F. Ham, and P. Moin, "Prediction of sound generated by complex flows at low Mach numbers," AIAA J. **48**(2), 306–316 (2010).
[36] J. D. Revell, R. A. Prydz, and A. P. Hays, "Experimental study of airframe noise vs. drag relationship for circular cylinders," Final report for NASA contract nas1-14403, Lockheed Report 28074, 1977.
[37] J. S. Cox, K. S. Brentner, and C. L. Rumsey, "Computation of vortex shedding and radiated sound for a circular cylinder: Subcritical to transcritical Reynolds numbers," Theor. Comput. Fluid Dyn. **12**, 233–253 (1998).